


Cite this: *RSC Adv.*, 2022, 12, 10258

# Continuous g-C<sub>3</sub>N<sub>4</sub> layer-coated porous TiO<sub>2</sub> fibers with enhanced photocatalytic activity toward H<sub>2</sub> evolution and dye degradation†

Jing Liu,<sup>a</sup> Jinxiao Zheng,<sup>b</sup> Guichu Yue,<sup>a</sup> Huaikeli,<sup>a</sup> Zhaoyue Liu,<sup>a</sup> Yong Zhao,<sup>a</sup> Nü Wang,<sup>a</sup> Chenghua Sun<sup>b</sup> and Zhimin Cui<sup>\*a</sup>

TiO<sub>2</sub>/g-C<sub>3</sub>N<sub>4</sub> composite photocatalysts with various merits, including low-cost, non-toxic, and environment friendliness, have potential application for producing clean energy and removing organic pollutants to deal with the global energy shortage and environmental contamination. Coating a continuous g-C<sub>3</sub>N<sub>4</sub> layer on TiO<sub>2</sub> fibers to form a core/shell structure that could improve the separation and transit efficiency of photo-induced carriers in photocatalytic reactions is still a challenge. In this work, porous TiO<sub>2</sub> (P-TiO<sub>2</sub>)/g-C<sub>3</sub>N<sub>4</sub> fibers were prepared by a hard template-assisted electrospinning method together with the g-C<sub>3</sub>N<sub>4</sub> precursor in an immersing and calcination process. The continuous g-C<sub>3</sub>N<sub>4</sub> layer was fully packed around the P-TiO<sub>2</sub> fibers tightly to form a TiO<sub>2</sub>@g-C<sub>3</sub>N<sub>4</sub> core/shell composite with a strong TiO<sub>2</sub>/g-C<sub>3</sub>N<sub>4</sub> heterojunction, which greatly enhanced the separation efficiency of photo-induced electrons and holes. Moreover, the great length-diameter ratio configuration of the fiber catalyst was favorable for the recycling of the catalyst. The P-TiO<sub>2</sub>@g-C<sub>3</sub>N<sub>4</sub> core/shell composite exhibited a significantly enhanced photocatalytic performance both in H<sub>2</sub> generation and dye degradation reactions under visible light irradiation, owing to the specific P-TiO<sub>2</sub>@g-C<sub>3</sub>N<sub>4</sub> core/shell structure and the high-quality TiO<sub>2</sub>/g-C<sub>3</sub>N<sub>4</sub> heterojunction in the photocatalyst. This work offers a promising strategy to produce photocatalysts with high efficiency in visible light through a rational structure design.

Received 18th February 2022

Accepted 18th March 2022

DOI: 10.1039/d2ra01093c

rsc.li/rsc-advances

## 1 Introduction

With rapid global industrialization and rapid population explosion, the global energy demand is ever growing. Traditional energy sources are non-renewable and thus exhaustible and also have hazardous combustion products, which put human beings under increasing threat from the energy dilemma and environmental contamination.<sup>1–3</sup> Therefore, it is highly desirable to explore new sources of energy that are sustainable and pollution-free. Among the many candidates, hydrogen energy derived from photocatalytic water decomposition is regarded as the most green and has great potential to substitute conventional fuels in terms of sustainability and cleanliness.<sup>4–8</sup> Besides, photocatalysts also show outstanding

performance for the degradation of contaminants in water and air.<sup>9–13</sup>

Among the numerous photocatalysts, TiO<sub>2</sub> has been extensively investigated due to its many outstanding advantages, including non-toxic nature, low-cost, pollution-free, chemical and thermal stability. However, the fast recombination of photo-induced carriers and its limited response to visible light greatly hinder its photocatalysis application. Hence, numerous efforts have been dedicated to the modification of TiO<sub>2</sub> for expanding its light absorption range and for separating the photogenerated holes and electrons rapidly, including surface sensitization, noble metal deposition, element doping, and heterojunction formation.<sup>14–17</sup> Graphitic carbon nitride (g-C<sub>3</sub>N<sub>4</sub>), a metalloid and polymeric photocatalyst, has shown great potential application in hydrogen production under visible light since 2009.<sup>18</sup> It has raised wide interested thanks to its excellent characteristics, for instance, chemical stability, cost-effectiveness, visible response, and environmental-friendly nature. The combination of TiO<sub>2</sub> and g-C<sub>3</sub>N<sub>4</sub> is a valid way to increase the separation efficiency of photon-induced carriers and expand the light absorption range.<sup>19,20</sup> Many avenues have been conducted to fabricate different morphologies of g-C<sub>3</sub>N<sub>4</sub>/TiO<sub>2</sub> nanocomposites. g-C<sub>3</sub>N<sub>4</sub>/TiO<sub>2</sub> nanosheet composites were fabricated by Keller *et al.* via a sol-gel and thermal

<sup>a</sup>Key Laboratory of Bioinspired Smart Interfacial Science and Technology of Ministry of Education, Beijing Key Laboratory of Bioinspired Energy Materials and Devices, School of Chemistry, Beijing Advanced Innovation Center for Biomedical Engineering, Beihang University, Beijing, 100191, P. R. China. E-mail: wangn@buaa.edu.cn; sunchenghua@mail.ipc.ac.cn; cuizhm@buaa.edu.cn

<sup>b</sup>Key Laboratory of Photochemical Conversion and Optoelectronic Materials, Technical Institute of Physics and Chemistry, Chinese Academy of Sciences, Beijing 100029, P. R. China

† Electronic supplementary information (ESI) available. See DOI: 10.1039/d2ra01093c



polycondensation synthesis. The nanocomposites exhibited efficient  $\text{H}_2$  production using very low amounts of sacrificial agents under visible light irradiation.<sup>21</sup> Song *et al.* mixed urea with  $\text{TiO}_2$  nanoparticles to fabricate coupled photocatalysts by calcination. The  $\text{TiO}_2/\text{g-C}_3\text{N}_4$  nanocomposite presented better photocatalytic phenol degradation performance.<sup>22</sup>  $\text{TiO}_2/\text{g-C}_3\text{N}_4$  nanospheres were fabricated by Wang *et al.* via a melt-infiltration of dicyandiamide into mesoporous  $\text{TiO}_2$  spheres followed by calcination. The melt-infiltration process made  $\text{g-C}_3\text{N}_4$  undergo better fusion into mesoporous  $\text{TiO}_2$  and formed a firm interfacial contact, which showed a higher performance for the visible light degradation of organic pollutants.<sup>23</sup> However, all these structures, such as nanosheets, nanoparticles, and nanospheres, are microscopic materials, which makes it difficult to recover and recycle the catalyst in practical application. Notably, fibers with a very large aspect ratio have structural advantages of a microscopic diameter as well as macroscopic length that make them very promising in catalyst recycling.

Among the various methods to fabricate fiber catalysts, electrospinning is a direct and effective approach to produce fibers with various fine structures.<sup>24–29</sup> Wang and Lei *et al.* synthesized  $\text{TiO}_2/\text{g-C}_3\text{N}_4$  nanocomposites by a simple electrospinning process. Few  $\text{g-C}_3\text{N}_4$  nanosheets were embedded and interspersed in the  $\text{TiO}_2$  nanofibers. The  $\text{TiO}_2/\text{g-C}_3\text{N}_4$  nanofibers showed improved photocatalytic activity for  $\text{H}_2$  evolution and rhodamine B (RhB) degradation under simulated solar irradiation.<sup>30</sup> Park and Kim *et al.* prepared  $\text{TiO}_2/\text{g-C}_3\text{N}_4$  nanofibers via a two-nozzle electrospinning process combined with a calcination method. The  $\text{TiO}_2/\text{g-C}_3\text{N}_4$  nanofibers showed significantly improved performance for the photocatalytic degradation of RhB and reactive black 5 under solar light irradiation.<sup>31</sup> However, the  $\text{g-C}_3\text{N}_4$  content among the composite is typically restricted, which means it is unable to form a large contacted interface with  $\text{TiO}_2$  in these methods. Li and Yan *et al.* synthesized a  $\text{TiO}_2/\text{g-C}_3\text{N}_4$  heterojunction nanofibers photocatalyst via electrospinning and an *in situ* evaporation calcination method to control the ratio of  $\text{g-C}_3\text{N}_4$  and  $\text{TiO}_2$  in the composite. The photocatalyst showed high activity in RhB degradation under simulated sunlight.<sup>32</sup> Wang *et al.* fabricated  $\text{TiO}_2/\text{g-C}_3\text{N}_4$  nanocomposites by combining electrospun  $\text{TiO}_2$  nanofibers and calcinated  $\text{g-C}_3\text{N}_4$  nanosheets with a hydrothermal reaction. The  $\text{TiO}_2/\text{g-C}_3\text{N}_4$  nanocomposites showed improved photocatalytic degradation performance for RhB solution.<sup>33</sup> However, the massive  $\text{g-C}_3\text{N}_4$  tended to aggregate on the  $\text{TiO}_2$  nanofibers. However, neither the blocks nor the adhesions of  $\text{g-C}_3\text{N}_4$  were negligible on account of the intrinsic agglomerating properties of  $\text{g-C}_3\text{N}_4$  on the  $\text{TiO}_2$  nanofibers during the calcination, which led to a limited surface area that is detrimental for forming homogeneous heterojunctions between  $\text{TiO}_2$  and  $\text{g-C}_3\text{N}_4$ . Heterojunction semiconductors achieved by infiltration approach method showed a greatly enhanced interfacial contact that surpassed that obtained by sol-gel chemistry or standard ball-milling methods.<sup>34</sup> Porous materials possesses abundant active sites for mass transfer to build heterojunction semiconductors through the high pore volumes and large surface areas. Here, the precursor could

facilely penetrate into the porous substrate material and nucleate, and then grow from inside to outside. As a result, substrate materials with a well-developed porosity could promote the growth of a secondary structure on the substrate to form strong contacted heterojunctions and could even enable a high structural stability.<sup>35,36</sup> In our previous work, hollow porous  $\text{TiO}_2/\text{g-C}_3\text{N}_4$  nanofiber photocatalysts were prepared via a coaxial electrospinning combined with infiltration method.<sup>37</sup> The hollow and porous  $\text{TiO}_2/\text{g-C}_3\text{N}_4$  nanofibers showed high photocatalytic performance for  $\text{H}_2$  evolution and RhB degradation, ascribed to the intact porous hollow structure and the  $\text{TiO}_2/\text{g-C}_3\text{N}_4$  heterojunctions. However, the  $\text{g-C}_3\text{N}_4$  layers grown on the  $\text{TiO}_2$  nanofiber were cocked, leading to an incomplete contact with the  $\text{TiO}_2$  substrate. In addition, the photocatalytic performance of the composite was confined due to the blocking of the hollow structure through the high  $\text{g-C}_3\text{N}_4$  content. Therefore, a continuous and uniform thin layer structure of  $\text{g-C}_3\text{N}_4$  on  $\text{TiO}_2$  fibers would be more favorable for the construction of intimate contacted  $\text{TiO}_2/\text{g-C}_3\text{N}_4$  heterojunctions, which would be highly beneficial for photocatalysis reactions because of the fast photocarrier separation superiority and large specific surface area.<sup>38–41</sup>

Herein, we developed a template-assisted electrospinning approach together with a solution infiltration process to coat a continuous  $\text{g-C}_3\text{N}_4$  layer on to porous  $\text{TiO}_2$  (P- $\text{TiO}_2$ ) fibers to produce a porous  $\text{TiO}_2@\text{g-C}_3\text{N}_4$  core/shell composite. Abundant mesopores in the  $\text{TiO}_2$  fibers provided accommodating venues for the precursor of  $\text{g-C}_3\text{N}_4$  in order that a continuous tightly wrapped  $\text{g-C}_3\text{N}_4$  shell could be grown on the P- $\text{TiO}_2$  fibers. Moreover, with the high content of  $\text{g-C}_3\text{N}_4$ , the porous  $\text{TiO}_2@\text{g-C}_3\text{N}_4$  composites still maintained the fibers' structure well with no aggregation or adhesion of  $\text{g-C}_3\text{N}_4$ . The intimate heterojunctions between the  $\text{g-C}_3\text{N}_4$  shell and P- $\text{TiO}_2$  fibers core inhibited the recombination of photo-induced carriers during the photocatalytic process. The  $\text{H}_2$  production and dye (RhB) degradation activities were both improved under visible light illumination, ascribed to the synergistic action of the continuous core/shell structure and the high-quality heterojunctions between the  $\text{g-C}_3\text{N}_4$  layers and  $\text{TiO}_2$  fibers.

## 2 Experimental

### 2.1 Materials

Polyvinylpyrrolidone (PVP,  $M_w = 1\,300\,000$ ) was provided by Aladdin (Shanghai, China). Titanium butoxide (TBOT), cyanamide (CY), triethanolamine (TEOA), acetylacetone, isopropanol (IPA), *p*-benzoquinone (*p*-BQ), RhB, methylene blue (MB), phenol and absolute ethanol were obtained from Macklin (Shanghai, China). The above reagents were all directly used without further treatment.

### 2.2 Fabrication of porous $\text{TiO}_2$ (P- $\text{TiO}_2$ ) fibers

P- $\text{TiO}_2$  fibers were produced via a template-assisted electrospinning technique. Hand-made candle soot carbon nanoparticles (CNPs) were used as the template to create nanopores in the  $\text{TiO}_2$  fibers. Generally, 1.2 g CNPs was added to 25.2 mL



ethanol and then ultrasonically processed for 2 h to disperse the CNPs uniformly. Next, 4.8 g PVP was mixed with the above solution with magnetic stirring for 6 h. Afterward, 1.0 g TBOT and 2.4 g acetylacetone were added to the above homogeneous PVP/CS ethanol solution and then stirred for 12 h to obtain the  $\text{TiO}_2$  precursor sol. The ejection rate of the spinning fluid was  $40 \mu\text{L min}^{-1}$ . The distance from the syringe needle to collector was 20 cm, and the voltage was 9.0 kV. The as-prepared fibers were calcined at  $500^\circ\text{C}$  for 3 h to prepare the P- $\text{TiO}_2$  fibers. Solid  $\text{TiO}_2$  (S- $\text{TiO}_2$ ) fibers with no nanopores were also fabricated by the same electrospinning condition without CNPs in the  $\text{TiO}_2$  precursor sol as a control to explore the role of nanopores in the formation of the  $\text{TiO}_2/\text{g-C}_3\text{N}_4$  core/shell structure.

### 2.3 Preparation of porous $\text{TiO}_2/\text{g-C}_3\text{N}_4$ (PTCN) core/shell heterojunction fiber photocatalysts

First, 0.5 mL cyanamide (CY) solution was added to the P- $\text{TiO}_2$  fibers dropwise to make CY solution infiltrate into the P- $\text{TiO}_2$  fibers fully and uniformly. The as-prepared mixture was transferred to a semi-enclosed silica crucible to calcinate at  $550^\circ\text{C}$  for 4 h. PTCN photocatalysts with different CY concentrations were tagged as PTCN- $x$  ( $x = 30\%, 70\%, 90\%$ ), where  $x$  represents the volume fraction of CY aqueous solution. As a control, the S- $\text{TiO}_2$  fibers were also treated by the same process to synthesize solid  $\text{TiO}_2/\text{g-C}_3\text{N}_4$  (STCN). Besides, pure  $\text{g-C}_3\text{N}_4$  was achieved *via* directly calcinating pristine CY under the same calcination conditions.

### 2.4 Characterization

The morphologies of the samples were inspected by scanning electron microscopy (SEM) (FEI Quanta FEG 250) with an acceleration voltage of 10 kV and by transmission electron microscopy (TEM) and high-resolution TEM (HRTEM) (JEM-F200). The Brunauer–Emmett–Teller (BET) surface areas ( $S_{\text{BET}}$ ) of the samples were determined using an ASAP 2420 (Micrometrics Instruments) nitrogen adsorption apparatus. The pore-size distributions were measured by the Barrett–Joyner–Halenda (BJH) model. X-ray diffraction (XRD) patterns were obtained on a Shimadzu XRD-6000, using a Cu  $K\alpha$  source. Fourier transform-infrared (FT-IR) spectra were obtained on a Thermo Scientific Nicolet 6700. X-ray photoelectron spectroscopy (XPS) analysis was performed on a Thermo Scientific ESCA Lab 250Xi. UV-Visible diffuse reflectance spectroscopy (DRS) was performed on a Shimadzu UV-3600. Photoluminescence (PL) spectra were obtained on a Cary Eclipse MY14110001. The UV-visible absorption spectra were obtained on an Agilent/Varian Cary 50.

### 2.5 Photocatalytic hydrogen evolution

The  $\text{H}_2$ -generation activity of the photocatalysts was characterized by a gas tracing and analysis system (Labsolar-6A, Beijing Perfectlight). Generally, the photocatalyst (50 mg) was dispersed in a mixture of distilled water (85 mL) and TEOA (15 mL) with constant stirring in a transparent quartz reactor. Next, 1 wt% Pt was loaded on to the photocatalyst by a photodeposition process. Previous to irradiation, the dissolved air in the reaction

system was removed by a vacuum pump. Subsequently, a xenon lamp (300 W,  $\lambda \geq 420 \text{ nm}$ ) (Microsolar 300, Beijing Perfectlight) was equipped to irradiate the photocatalysts suspension. The gaseous product was sampled and analyzed directly by gas chromatography (Techcomp, GC-7900) with an argon gas carrier. The reaction system was kept at  $5^\circ\text{C}$  by recirculating water.

### 2.6 Photocatalytic degradation

The photodegradations of RhB (10 ppm), MB (10 ppm), and phenol (5 ppm) were employed to characterize the catalytic activity of the photocatalysts under visible light irradiation. Generally, 50 mg catalyst was added to 50 mL RhB (MB and phenol) solution. Before irradiation, the reaction solution was continuously stirred at  $25^\circ\text{C}$  for 60 min in the dark to establish adsorption–desorption equilibrium. Next, 3.5 mL of RhB (MB and phenol) solution was extracted periodically to record the concentration change of RhB by the UV-vis absorbance spectrum at 553 nm (664 nm for MB and 270 nm for phenol).  $C/C_0$  was calculated, where  $C_0$  represents the initial concentration of RhB solution after the adsorption–desorption process,  $C$  stands for the real-time RhB concentration under visible light. The photocatalyst was recovered and reused in repeat cycles to investigate the stability. Moreover, different scavengers were used to explore the photocatalytic degradation mechanism of the core/shell PTCN composite. Before the reaction,  $p\text{-BQ}$  (0.25 mM), IPA (1 mM), and TEOA (1 mM) were injected in to the RhB solution, respectively, to trap superoxide radicals ( $\text{O}_2^{\cdot-}$ ), hydroxyl radicals ( $\text{OH}^\cdot$ ), and holes ( $\text{h}^+$ ) species.

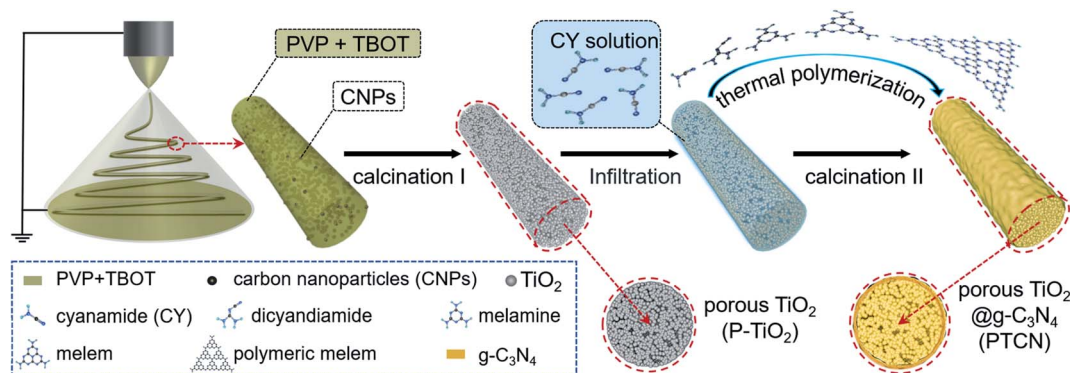
## 3 Results and discussion

Scheme 1 exhibits a diagrammatic sketch for the preparation of porous  $\text{TiO}_2/\text{g-C}_3\text{N}_4$  (PTCN) fibers with the core/shell structure. The P- $\text{TiO}_2$  fibers were constructed *via* a carbon nanoparticles (CNPs) template-assisted electrospinning approach. The electrospinning fluid was a mixture of home-made candle soot CNPs, PVP, and TBOT. The CNPs with an average diameter of 30 nm served as a template to produce the porous structure (Fig. S1a†). During the first calcination step, the organics and CNPs were removed and thus porous  $\text{TiO}_2$  (P- $\text{TiO}_2$ ) fibers were obtained. After immersing the P- $\text{TiO}_2$  fibers in a certain concentration of cyanamide (CY) solution, followed by second calcination step, PTCN fibers with a core/shell structure were obtained.

Fig. 1a–f display the evolution process from electrospinning the precursor fibers to PTCN core/shell fibers with different  $\text{g-C}_3\text{N}_4$  contents. The precursor fibers had a relatively smooth appearance with a few CNPs on the surface (Fig. 1a). The calcinated fibers exhibited an incompact and porous surface after removing PVP and CNPs (Fig. 1b and S1b†). The pore size of the P- $\text{TiO}_2$  fibers matched well with the particle size of the CNPs template (Fig. S1c and d†) and the diameter of the P- $\text{TiO}_2$  fiber was approximately  $1.08 \mu\text{m}$  (Fig. S1f†). After the secondary calcination step, the CY underwent a thermal polymerization process and formed a continuous  $\text{g-C}_3\text{N}_4$  thin layer on the PTCN







**Scheme 1** Scheme for the preparation of porous  $\text{TiO}_2\text{@g-C}_3\text{N}_4$  (PTCN) core/shell fibers. Porous  $\text{TiO}_2$  (P- $\text{TiO}_2$ ) fibers were produced via a template-assisted electrospinning technique with subsequent calcination. Then, the P- $\text{TiO}_2$  fibers were immersed in cyanamide (CY) solution followed by a second step of calcination to prepare PTCN with a core/shell structure.

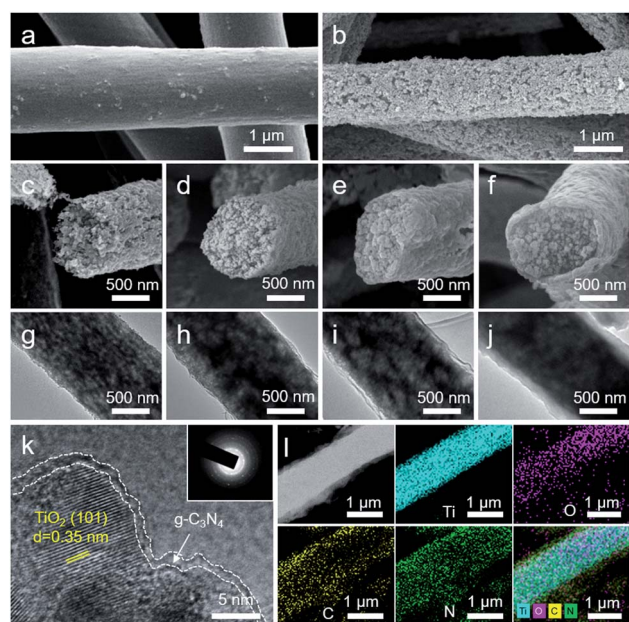


**Fig. 1** SEM images of (a) pristine electrospinning fibers and (b) P- $\text{TiO}_2$  fibers. (c–f) Cross section images of P- $\text{TiO}_2$ , PTCN-30%, PTCN-70%, and PTCN-90%. (g–j) TEM images of P- $\text{TiO}_2$ , PTCN-30%, PTCN-70%, and PTCN-90%. The  $\text{g-C}_3\text{N}_4$  shell of PTCN became more contiguous and thicker apparently with the increase in CY concentration. (k) HRTEM image of PTCN-90% (the inset exhibits the SAED pattern of PTCN-90%, indicating the polycrystalline configuration). (l) HAADF-STEM image and EDX mapping images of elemental Ti, O, C, N and a layer image of a single PTCN-90% fiber. Mesopores homogeneously distributed in the PTCN-90% core/shell fiber. The distribution of four elements in the fiber further confirmed the formation of the  $\text{TiO}_2\text{@g-C}_3\text{N}_4$  core/shell structure.

fibers. The cross-section SEM and TEM images revealed the detailed structures of the P- $\text{TiO}_2$  and PTCN fibers. The P- $\text{TiO}_2$  fibers were composed of small nanoparticles (Fig. 1c and g). Layered  $\text{g-C}_3\text{N}_4$  could be observed from all the PTCN samples (PTCN-30%, 70%, and 90%). When the concentration of CY solution was 30%, a very thin layer about 36 nm thick was detected around the outside of the P- $\text{TiO}_2$  fibers (Fig. 1d and h).

As the CY concentration increased to 70%, the outer shell of the fiber became distinct with a thickness of about 50 nm (Fig. 1e and i). When the CY concentration was up to 90%, a dense and continuous shell of approximately 85 nm thickness was wrapped around the P- $\text{TiO}_2$  fiber tightly (Fig. 1f and j). The surface SEM image also showed the  $\text{g-C}_3\text{N}_4$  shell covers around the P- $\text{TiO}_2$  fiber became thicker and denser as the CY concentration increased (Fig. S2†). The digital photos of all samples presented a gradual color change from white to yellow with the increase in CY concentration (Fig. S3†). Fig. 1k shows the high-resolution TEM (HRTEM) image of the PTCN-90% composite. The boundary of a  $\text{TiO}_2$  crystalline grain with a lattice fringe of 0.35 nm was coherent with the anatase  $\text{TiO}_2(101)$  lattice plane (Fig. 1k and S1e†).<sup>32</sup> A thin  $\text{g-C}_3\text{N}_4$  layer could be observed around the  $\text{TiO}_2$  grain, which was the  $\text{g-C}_3\text{N}_4$  phase.<sup>42</sup> In the inset of Fig. 1k, the selected area electron diffraction pattern (SAED) of HPCN-90% revealed the polycrystalline configuration of the  $\text{TiO}_2/\text{g-C}_3\text{N}_4$  heterojunction. The HAADF-STEM image and EDX elemental mapping images of PTCN-90% are shown in Fig. 1l. The broader distribution range of C and N agreed well with the  $\text{TiO}_2\text{@g-C}_3\text{N}_4$  core/shell structure, while the overlapping distribution range of Ti, O, C, and N indicated that an intimate  $\text{TiO}_2/\text{g-C}_3\text{N}_4$  heterojunction was also constructed in the P- $\text{TiO}_2$  fiber together with the continuous  $\text{g-C}_3\text{N}_4$  coating.

As contrast, solid  $\text{TiO}_2$  (S- $\text{TiO}_2$ ) fiber@ $\text{g-C}_3\text{N}_4$  (STCN) nanostructures were also prepared to investigate the effect of the nanopores in  $\text{TiO}_2$  fiber for the growth of the  $\text{g-C}_3\text{N}_4$  coating. S- $\text{TiO}_2$  fibers were fabricated by almost the same electrospinning method but without the CNPs template. After the first calcination step, only tiny holes could be observed on the surface of the S- $\text{TiO}_2$  fibers (Fig. S4a†). After immersing the S- $\text{TiO}_2$  fibers in a certain concentration of CY solution and followed by a second calcination step, the STCN composite was obtained. However, plenty of separate  $\text{g-C}_3\text{N}_4$  nanosheets could be observed by the side of the S- $\text{TiO}_2$  fiber in the STCN composite (Fig. S4b†). Although a small amount of  $\text{g-C}_3\text{N}_4$  was coated on the S- $\text{TiO}_2$  fibers, a continuous  $\text{g-C}_3\text{N}_4$  layer was not formed like in PTCN (Fig. S4c†). This significant difference was because  $\text{g-C}_3\text{N}_4$  is easy to agglomerate on S- $\text{TiO}_2$  fibers during calcination at high



temperature, while the porous structure of P-TiO<sub>2</sub> makes CY solution easily infiltrate into the internal structure of the TiO<sub>2</sub> fibers and hence forms a continuous g-C<sub>3</sub>N<sub>4</sub> shell layer around the P-TiO<sub>2</sub> fibers core. Apparently, the porous structure of P-TiO<sub>2</sub> fibers is not only crucial for the intimate contact between TiO<sub>2</sub> fibers and g-C<sub>3</sub>N<sub>4</sub>, but also significant for the continuous g-C<sub>3</sub>N<sub>4</sub> coating on the TiO<sub>2</sub> fibers.

X-ray diffraction (XRD) patterns were measured to investigate the crystal phases of TiO<sub>2</sub>, g-C<sub>3</sub>N<sub>4</sub>, and PTCN-90% (Fig. 2a). The diffraction peaks at 25.1°, 37.7°, and 47.9° corresponded to the (101), (004), and (221) lattice planes of anatase TiO<sub>2</sub> (JCPDS no. 21-1272). The characteristic peak of g-C<sub>3</sub>N<sub>4</sub> was located at 27.5°, corresponding to the (002) diffraction plane.<sup>23</sup> The peak intensity of g-C<sub>3</sub>N<sub>4</sub> in the PTCN became stronger with the increase in CY concentration from 30% to 90%, indicating a more crystalline g-C<sub>3</sub>N<sub>4</sub> was grown in the P-TiO<sub>2</sub> fibers (Fig. S5a†). The FT-IR spectra of the TiO<sub>2</sub>, g-C<sub>3</sub>N<sub>4</sub>, and PTCN-90% heterojunction photocatalysts are presented in Fig. 2b. In the range of 700–900 cm<sup>−1</sup>, TiO<sub>2</sub> exhibited a wide band because of the Ti–O–Ti stretching vibration. Pure g-C<sub>3</sub>N<sub>4</sub> displayed three feature adsorption regions located at 3000–3500, 1200–1700, and 810 cm<sup>−1</sup>, respectively. The broad adsorption region around 3000–3500 cm<sup>−1</sup> was indexed to the N–H typical stretching vibration. The strong feature peaks between 1200 to 1700 cm<sup>−1</sup> were attributed to the C–N heterocycles stretching vibration. Moreover, the sharp absorption peak at 810 cm<sup>−1</sup> was

related to the specific triazine units breathing mode.<sup>43</sup> In the FT-IR spectra of PTCN-90%, we could easily find the characteristic peaks for TiO<sub>2</sub> and g-C<sub>3</sub>N<sub>4</sub> in the relevant positions, which indicated that g-C<sub>3</sub>N<sub>4</sub> was formed in PTCN fiber. With the concentration of CY increasing from 30% to 90%, the peak intensity of g-C<sub>3</sub>N<sub>4</sub> became stronger in the PTCN heterojunction photocatalysts (Fig. S5b†). N<sub>2</sub> adsorption–desorption isotherms were obtained and showed that all the samples presented type IV isotherms (Fig. 2c and S7a†). S-TiO<sub>2</sub> exhibited an H2 hysteresis loop, illustrating that the S-TiO<sub>2</sub> fiber possessed uniform intergranular pores (Fig S6a†). P-TiO<sub>2</sub> and PTCN-90% showed H2 and H3 hysteresis loops, indicating the existence of inkbottle pores and slit-shaped pores, resulting from interconnected pore channels and plate-like particles aggregation. Only a type H3 hysteresis loop was observed in g-C<sub>3</sub>N<sub>4</sub>, owing to its layered structure.<sup>44,45</sup> P-TiO<sub>2</sub> had a larger *S*<sub>BET</sub> of 53.71 m<sup>2</sup> g<sup>−1</sup>, which was 1.48 times that of S-TiO<sub>2</sub> (36.25 m<sup>2</sup> g<sup>−1</sup>) owing to the introduction of mesopores in the electrospun TiO<sub>2</sub> fibers. Compared to P-TiO<sub>2</sub>, the *S*<sub>BET</sub> of the PTCN-90% sample (22.85 m<sup>2</sup> g<sup>−1</sup>) clearly dropped, ascribed to the coating of the g-C<sub>3</sub>N<sub>4</sub> layer on the P-TiO<sub>2</sub> nanopores. The coated g-C<sub>3</sub>N<sub>4</sub> layer blocks part of the nanopores and nanocavities of PTCN-90%. By comparison, pure g-C<sub>3</sub>N<sub>4</sub> presented the lowest *S*<sub>BET</sub> of 13.20 m<sup>2</sup> g<sup>−1</sup> (Table S1†). A main pore-size distribution around 10–15 nm was detected in S-TiO<sub>2</sub>, ascribed to the thermal decomposition of organic substances in the process of the calcination. P-TiO<sub>2</sub> exhibited a larger pore diameter and wider pore distribution than S-TiO<sub>2</sub>, owing to the abundant pore structure in the fibers (Fig. S6b†). As shown in Fig. 2d and S7b,† PTCN-90% showed a much lower pore volume than P-TiO<sub>2</sub>, PTCN-30%, and PTCN-90%, on account of filling up the plentiful g-C<sub>3</sub>N<sub>4</sub> nanosheets into the nanopores of P-TiO<sub>2</sub>. The pore-size distribution results coincided with the *S*<sub>BET</sub> and morphology characterization results.

X-ray photoelectron spectroscopy (XPS) was performed to further explore the compositions and surface chemical status of the obtained photocatalysts. C, N, Ti, and O elements were all detected in the spectra of PTCN-90%, which was consistent with the EDX results (Fig. S8a†). Fig. 2e displays the N 1s high-resolution spectrum of PTCN-90% with g-C<sub>3</sub>N<sub>4</sub> for comparison. N 1s peaks at 398.4, 398.9, and 400.9 eV were ascribed to the sp<sup>2</sup>-hybridized nitrogen of triazine rings (C=N–C), tertiary nitrogen ((C)<sub>3</sub>–N), and nitrogen in the amino functional groups (C–N–H), respectively. The isolated peak at 403.3 eV was attributed to the charging effect or a positive charge localization in the heterocycles.<sup>30</sup> The binding energy of N–(C)<sub>3</sub> (398.9 eV) showed a slight negative shift of 0.2 eV by contrast with g-C<sub>3</sub>N<sub>4</sub> (399.1 eV), confirming the strong interfacial interaction between the TiO<sub>2</sub> fiber and g-C<sub>3</sub>N<sub>4</sub> layer rather than a simple physical mixing.<sup>44</sup> The C 1s spectral peaks in PTCN-90% at 284.8 and 288.0 eV represented the sp<sup>2</sup>-hybridized carbon (N–C=N) groups and graphitic carbon (C–C), respectively (Fig. S8b†). A negative shift of 0.1 eV compared with pure g-C<sub>3</sub>N<sub>4</sub> was observed, attributed to the interaction effect of O–Ti–O–C–N bonds between g-C<sub>3</sub>N<sub>4</sub> and TiO<sub>2</sub>.<sup>21</sup> The O 1s peaks at 530.2 and 531.6 eV in HPCN-90% were associated with Ti–O and Ti–OH (Fig. 2e). Fig. S8c† displays the Ti 2p high-resolution

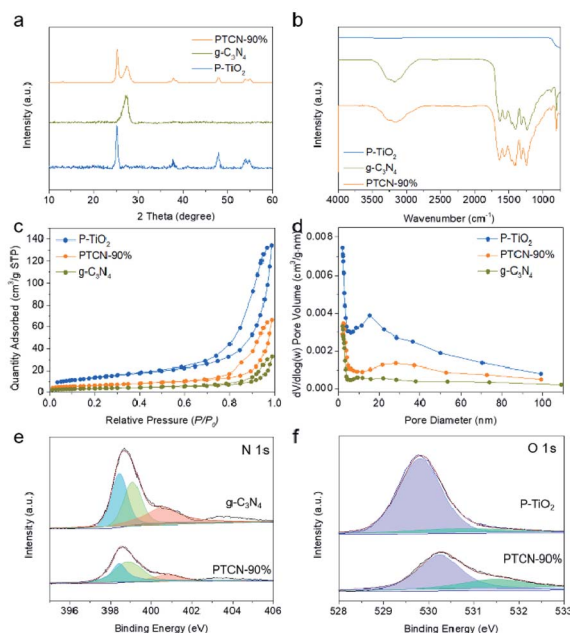


Fig. 2 (a and b) XRD patterns and FT-IR spectra for P-TiO<sub>2</sub>, g-C<sub>3</sub>N<sub>4</sub>, and PTCN-90%. The characteristic peaks of TiO<sub>2</sub> and g-C<sub>3</sub>N<sub>4</sub> were both found in PTCN-90%, indicating g-C<sub>3</sub>N<sub>4</sub> was successfully coupled on the TiO<sub>2</sub> fibers. (c and d) The N<sub>2</sub> adsorption–desorption isotherms and corresponding pore-size distributions of P-TiO<sub>2</sub>, PTCN-90%, and g-C<sub>3</sub>N<sub>4</sub>. Both *S*<sub>BET</sub> and pore volume of PTCN-90% decrease apparently compared with P-TiO<sub>2</sub>, due to the filling of g-C<sub>3</sub>N<sub>4</sub> in to the nanopores of the P-TiO<sub>2</sub> fibers. (e and f) High-resolution XPS spectra of N 1s and O 1s of PTCN-90%, g-C<sub>3</sub>N<sub>4</sub>, and P-TiO<sub>2</sub>.



spectrum. The two peaks at 459.0 and 464.7 eV corresponded to Ti 2p<sub>3/2</sub> and Ti 2p<sub>1/2</sub> and originated from the spin orbit interaction, indicating that the Ti ions were tetravalent.<sup>46</sup> Apparently positive shifts in the binding energies in Ti 2p and O 1s were observed, confirming the intimate contact of the g-C<sub>3</sub>N<sub>4</sub> layer and P-TiO<sub>2</sub> fiber in HPCN-90%. The high-quality TiO<sub>2</sub>/g-C<sub>3</sub>N<sub>4</sub> heterojunction is crucial to accelerate the separation and transport of photo-induced electrons and holes.<sup>46,47</sup>

Photocatalytic H<sub>2</sub> production performance measurements of all the samples were conducted under a xenon lamp (300 W,  $\lambda \geq 420$  nm). A 1 wt% platinum (Pt) loading on the photocatalysts was performed by a photodeposition method to serve as a cocatalyst. As shown in Fig. 3a and b, P-TiO<sub>2</sub> had almost no photocatalytic activity for H<sub>2</sub> production under visible light irradiation, due to its limited photoresponse to visible light. Pure g-C<sub>3</sub>N<sub>4</sub> showed a lower H<sub>2</sub> evolution rate on account of the fast recombination of photo-induced carriers.<sup>48</sup> All the PTCN samples showed a higher H<sub>2</sub> production rate when compared with that of P-TiO<sub>2</sub> and g-C<sub>3</sub>N<sub>4</sub> under visible light. The H<sub>2</sub>-production efficiency gradually improved with the increase in CY concentration. To further investigate the influence of the photocatalyst structure on H<sub>2</sub> evolution, the photocatalytic H<sub>2</sub>-generation performances of g-C<sub>3</sub>N<sub>4</sub>, P-TiO<sub>2</sub>, STCN-90%, and PTCN-90% were assessed and are depicted in Fig. 3c. STCN-90% and PTCN-90% showed evidently higher H<sub>2</sub> performances compared to g-C<sub>3</sub>N<sub>4</sub> and TiO<sub>2</sub>. The photocatalytic H<sub>2</sub>-evolution rate of STCN-90% was 310  $\mu\text{mol g}^{-1} \text{h}^{-1}$ , which was 4.4 times as much as that of g-C<sub>3</sub>N<sub>4</sub> (70  $\mu\text{mol g}^{-1} \text{h}^{-1}$ ). This demonstrated that the combination of TiO<sub>2</sub> and g-C<sub>3</sub>N<sub>4</sub> favored improving the photocatalytic H<sub>2</sub>-evolution rate. PTCN-90% presented the highest rate of 436  $\mu\text{mol g}^{-1} \text{h}^{-1}$ , which was 6.2 times higher than that of pure g-C<sub>3</sub>N<sub>4</sub>. The H<sub>2</sub>-evolution rate of PTCN-90% was improved by 40.6% when compared with STCN-90%,

indicating that the intimate core/shell heterojunction with a continuous g-C<sub>3</sub>N<sub>4</sub> layer played an important role in the photocatalytic H<sub>2</sub>-evolution performance. The reductions of the H<sub>2</sub>-production efficiency and structures were not significantly impacted after four cycles tests, demonstrating the great recyclability of PTCN-90% (Fig. 3d and S9†). The g-C<sub>3</sub>N<sub>4</sub> layer still adhered to the TiO<sub>2</sub> fibers firmly, which confirmed the high stability of the PTCN-90% photocatalyst. When comparing the different TiO<sub>2</sub>/g-C<sub>3</sub>N<sub>4</sub> composite photocatalysts with other structures, such as nanowires, nanospheres, and nanosheets, the PTCN photocatalyst still exhibited an excellent H<sub>2</sub>-evolution performance (Table S2†).

The photocatalytic RhB degradation activities of all the samples were characterized under visible light irradiation with a wavelength longer than 420 nm. The photodegradation of RhB was negligible in the absence of the photocatalyst. All the PTCN photocatalysts exhibited higher activity for RhB degradation than P-TiO<sub>2</sub> and g-C<sub>3</sub>N<sub>4</sub>. Especially, PTCN-90% showed the best RhB photodegradation performance, with the complete degradation of RhB in 30 min (Fig. 4a). The photocatalytic degradation reaction conformed to pseudo-first-order kinetics described as  $-\ln(C/C_0) = kt$ , where  $k$  stands for the pseudo-first-order rate constant, which corresponds to the fitting line slope,

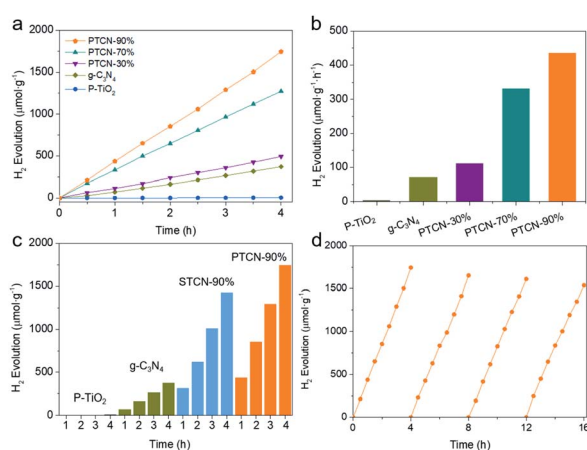


**Fig. 3** (a and b) Time courses of H<sub>2</sub> generation and average generation rate of P-TiO<sub>2</sub>, g-C<sub>3</sub>N<sub>4</sub>, PTCN-30%, PTCN-70%, and PTCN-90% under visible-light irradiation. With the increase in CY concentration, the photocatalytic hydrogen generation efficiency of PTCN was improved. (c) Time courses of H<sub>2</sub> generation of P-TiO<sub>2</sub>, g-C<sub>3</sub>N<sub>4</sub>, STCN-90%, and PTCN-90%. The intimate core/shell in PTCN-90% was beneficial to enhancing the H<sub>2</sub>-generation efficiency. (d) Cyclic runs for the photocatalytic H<sub>2</sub> evolution of PTCN-90%.

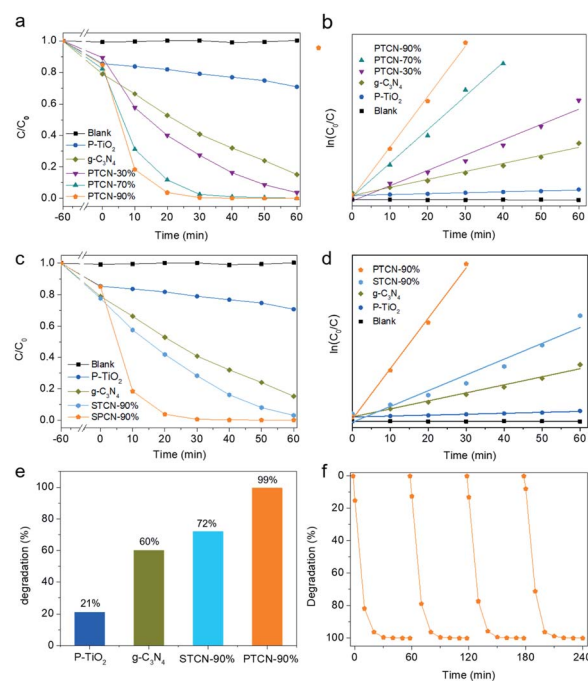


**Fig. 4** (a and b) Photocatalytic RhB degradation performance and degradation kinetic curves of P-TiO<sub>2</sub>, g-C<sub>3</sub>N<sub>4</sub>, PTCN-30%, PTCN-70%, and PTCN-90% under visible light irradiation. The RhB degradation rate was improved by raising the content of g-C<sub>3</sub>N<sub>4</sub>. PTCN-90% possessed the highest RhB degradation rate. (c and d) RhB photocatalytic degradation performance and degradation kinetic curves for P-TiO<sub>2</sub>, g-C<sub>3</sub>N<sub>4</sub>, STCN-90%, and PTCN-90%. (e) RhB photocatalytic degradation efficiency of P-TiO<sub>2</sub>, g-C<sub>3</sub>N<sub>4</sub>, STCN-90%, and PTCN-90% in 30 min. PTCN-90% had a much higher RhB degradation rate than STCN-90% due to the continuous core/shell structure advantage in PTCN. (f) Cyclic runs for RhB degradation over PTCN-90%.



and  $C_0$  and  $C$  represent the solution concentrations at time 0 and  $t$ , respectively. The kinetic curves of all the samples for photocatalytic RhB degradation are demonstrated in Fig. 4b. PTCN-90% had the highest  $k$  value of  $0.1674 \text{ min}^{-1}$ , which was 54 times that of  $\text{TiO}_2$  ( $0.0030 \text{ min}^{-1}$ ) and 6.3 times that of  $\text{g-C}_3\text{N}_4$  ( $0.0267 \text{ min}^{-1}$ ). In order to verify the effect of the intimate core/shell structure in PTCN, the photocatalytic RhB photodegradation performance and degradation kinetic curves for P-TiO<sub>2</sub>, g-C<sub>3</sub>N<sub>4</sub>, STCN-90%, and PTCN-90% were also assessed (Fig. 4c and d). The degradation rate of PTCN-90% was significantly higher than for STCN-90% ( $0.0524 \text{ min}^{-1}$ ) due to the specific core/shell structure and strong heterojunction between TiO<sub>2</sub> and g-C<sub>3</sub>N<sub>4</sub>. In 30 min, RhB was degraded almost completely by PTCN-90%; however, it could only be degraded 72% by STCN-90% (Fig. 4e). The corresponding changes in the UV-vis absorption spectra and optical images of RhB solution are exhibited in Fig. S10.† The absorption peak of the PTCN-90% sample dropped rapidly with prolonging the irradiation time and disappeared completely after 30 min. The inset shows the color change of RhB solution. The stability analysis of PTCN-90% for RhB degradation was also conducted by the recycling experiment (Fig. 4f). The performance of RhB degradation did not change obviously within four cycles, demonstrating the stability of the PTCN heterojunction photocatalyst. The core/shell PTCN-90% photocatalyst also exhibited good degradation performance for MB, in addition to RhB (Fig. S11†), where 10 ppm MB solution was completely degraded within 50 min by PTCN-90% under visible light irradiation. In consideration of the decolorization of dyes caused by a self-sensitization mechanism,<sup>49,50</sup> phenol, which has no photosensitization, was selected as the substrate to further investigate the photocatalytic performance of the core/shell PTCN-90% photocatalyst (Fig. S12†). The core/shell PTCN-90% photocatalyst also exhibited good degradation performance for phenol, which was completely degraded within 3.5 h under visible light irradiation. This proved that the core/shell PTCN photocatalyst has wide application prospects in the field of photocatalysis for organic pollutant degradation.

To further explore the photodegradation mechanism of RhB, active material trapping experiments were conducted (Fig. 5a). Superoxide radicals ( $\cdot\text{O}_2^-$ ), photoexcited holes ( $\text{h}^+$ ), and hydroxyl radicals ( $\cdot\text{OH}$ ) generated in the photocatalytic system could be shielded by *p*-BQ, TEOA, and IPA, respectively.<sup>12</sup> The RhB degradation decline of PTCN-90% was not significant with the presence of IPA. However, the degradation effect dramatically decreased when TEOA was added. This demonstrated that  $\text{h}^+$  was the dominant active species in the photodegradation reaction of RhB. Moreover, the  $\cdot\text{O}_2^-$  derived from dissolved  $\text{O}_2$  also acted as a partial player in the photocatalytic system. Photoluminescence (PL) emission spectroscopy is the most intuitive detection method to determine the separation efficiency of photo-induced carriers. The PL spectra for P-TiO<sub>2</sub>, g-C<sub>3</sub>N<sub>4</sub>, and PCN-90% were evaluated with an excitation wavelength of 320 nm (Fig. 5b).<sup>51</sup> It was revealed that g-C<sub>3</sub>N<sub>4</sub> had a strong peak at 470 nm related to the band-band PL phenomenon.<sup>52</sup> The bandgap energy was almost equal to the emission light energy of g-C<sub>3</sub>N<sub>4</sub>.<sup>53</sup> The emission peak of the

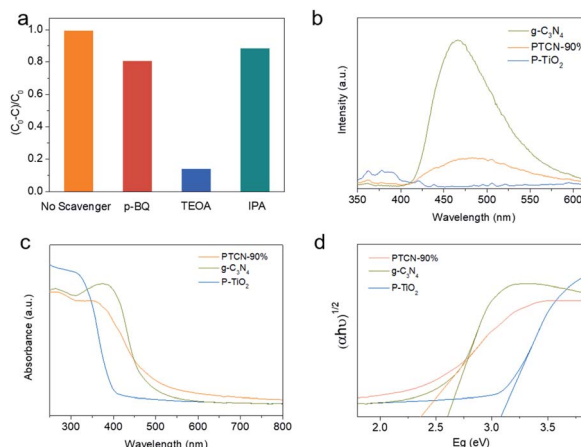
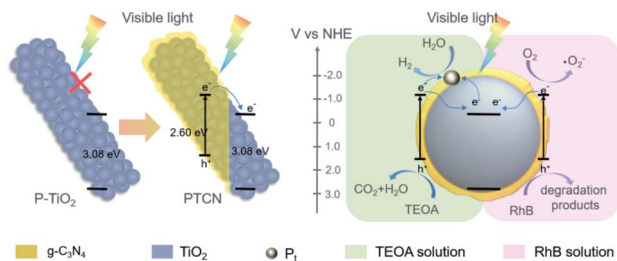


Fig. 5 (a) Active species trapping during RhB photodegradation over PTCN-90% under visible light irradiation for 30 min. (b) PL spectra of PTCN-90%, g-C<sub>3</sub>N<sub>4</sub>, and P-TiO<sub>2</sub>. The strong heterojunction between g-C<sub>3</sub>N<sub>4</sub> and TiO<sub>2</sub> accelerated the separation and transportation rate of photo-induced carriers. (c) DRS spectra and (d) corresponding band gap energy of PTCN-90%, g-C<sub>3</sub>N<sub>4</sub>, and P-TiO<sub>2</sub>. A significant red-shift of absorption was observed in PTCN-90%, suggesting the close mutual effect between the g-C<sub>3</sub>N<sub>4</sub> layer and P-TiO<sub>2</sub> fibers.

PTCN-90% heterojunction photocatalyst was weaker than for g-C<sub>3</sub>N<sub>4</sub>, which proved that PTCN-90% had a higher photo-induced carriers separation rate by virtue of the heterojunction between g-C<sub>3</sub>N<sub>4</sub> and P-TiO<sub>2</sub>. These results explain well its enhanced photocatalytic performance in photocatalytic H<sub>2</sub> generation and dye degradation.<sup>54</sup> Next, UV-visible diffuse reflectance spectroscopy (DRS) was performed to understand the optical absorption property of the photocatalysts. The DRS absorption edge of pure TiO<sub>2</sub> was 398 nm, implying that pure TiO<sub>2</sub> only has a response in the UV region; while g-C<sub>3</sub>N<sub>4</sub> presented a wider absorption in the visible and UV region with the absorption edge of 450 nm. PTCN-90% showed an obvious absorption extension to the visible region compared to that of pure TiO<sub>2</sub> (Fig. 5c).<sup>13</sup> The absorption extension of PTCN was ascribed to the strong heterojunction between g-C<sub>3</sub>N<sub>4</sub> and P-TiO<sub>2</sub> in the composites. A close-contacted core-shell structure and heterojunction in PTCN catalysts are favorable for separating the photogenerated electrons rapidly, which is highly conducive to accelerating photocatalytic reactions. The band gap energy of photocatalysts could be calculated by  $E_g = 1240/\lambda_g$ , where  $E_g$  is the bandgap energy and  $\lambda_g$  is the edge of optical absorption.<sup>55</sup> The calculated band gap energy of TiO<sub>2</sub>, g-C<sub>3</sub>N<sub>4</sub> and PTCN-90% were 3.08, 2.60, and 2.37 eV, respectively (Fig. 5d). The PTCN-90% core/shell photocatalyst presented the narrowest band gap compared with P-TiO<sub>2</sub> and g-C<sub>3</sub>N<sub>4</sub>, indicating its higher responsive to visible light.

A reasonable mechanism is proposed to illustrate the improved performance of the PTCN core/shell photocatalyst (Scheme 2). The  $E_{CB}$  and  $E_{VB}$  values of TiO<sub>2</sub> were calculated to be  $-0.23$  and  $2.85$  eV. Correspondingly, the  $E_{CB}$  and  $E_{VB}$  values of g-C<sub>3</sub>N<sub>4</sub> were  $-1.08$  and  $1.52$  eV, respectively.<sup>56</sup> TiO<sub>2</sub> had a limited absorption range in the UV light area and no response in the visible region due to the broad band gap. However, the coating





**Scheme 2** Proposed mechanism in PTCN fibers for photocatalytic H<sub>2</sub> evolution and RhB degradation. Under visible light irradiation, P-TiO<sub>2</sub> had no photocatalytic response, due to its broad band gap. While in the core/shell PTCN composite, photogenerated electrons in the g-C<sub>3</sub>N<sub>4</sub> shell could transfer to the P-TiO<sub>2</sub> core rapidly through the heterojunction, thereby realizing effective electron–hole separation. For the H<sub>2</sub>-evolution process, electrons accumulate on Pt particles and participate in the water splitting reaction. For the RhB degradation reaction, the photogenerated holes and the superoxide radicals derived from the dissolved O<sub>2</sub> are responsible for RhB degradation.

of a continuous g-C<sub>3</sub>N<sub>4</sub> layer on P-TiO<sub>2</sub> fibers to construct the PTCN heterojunction could broaden its light absorption range. Under visible light conditions, the photo-induced electrons separate, with the holes rapidly leaping to the g-C<sub>3</sub>N<sub>4</sub> CB, and then transiting to the CB of TiO<sub>2</sub> readily through the TiO<sub>2</sub>/g-C<sub>3</sub>N<sub>4</sub> heterojunction in PTCN. The fast separate and transfer of the electrons inhibit the recombination of carriers efficiently. As the reaction progresses, more electrons gather in the TiO<sub>2</sub> CB and more holes stay in g-C<sub>3</sub>N<sub>4</sub> VB. In the process of photocatalytic water splitting, electrons accumulate on the cocatalyst and reduce H<sup>+</sup> to H<sub>2</sub>. Photogenerated holes in g-C<sub>3</sub>N<sub>4</sub> VB oxidize TEOA to CO<sub>2</sub> and H<sub>2</sub>O. Moreover, during the RhB photo-degradation process, a portion of dissolved O<sub>2</sub> is reduced by electrons to create superoxide radicals with a high oxidation ability in the CB of g-C<sub>3</sub>N<sub>4</sub>. According to the active species trapping experiments, the photoexcited holes together with superoxide radicals acted as reactive species to decompose RhB into its degradation products. As a consequence, the strong heterojunction between g-C<sub>3</sub>N<sub>4</sub> and TiO<sub>2</sub> together with the intimate core/shell fiber structure facilitate the transport of photoexcited carriers. The unique TiO<sub>2</sub>/g-C<sub>3</sub>N<sub>4</sub> core/shell structure and the TiO<sub>2</sub>/g-C<sub>3</sub>N<sub>4</sub> heterojunction produce a synergistic effect to the photocatalytic efficiency in the PTCN composite.

## 4 Conclusions

TiO<sub>2</sub>@g-C<sub>3</sub>N<sub>4</sub> core/shell fibers were fabricated by a template-assisted electrospinning method together with a solution infiltration process. In the synthesis process, the porous structure of the TiO<sub>2</sub> fibers enabled CY solution to readily immerse into the abundant nanopores and nanocavities to build a continuous and close-contacted TiO<sub>2</sub> core/g-C<sub>3</sub>N<sub>4</sub> shell structure. The strong heterojunction between TiO<sub>2</sub> and g-C<sub>3</sub>N<sub>4</sub> accelerated the separation and transfer of photoexcited electrons and holes rapidly. In addition, the intimate core/shell structure provided a rapid transmission channel for carriers as well. The

synergistic effect of the strong heterojunction and intimate core/shell structure of the PTCN composite photocatalyst led to a significant improvement in the photocatalytic performance. PTCN-90% exhibited the highest performance in H<sub>2</sub> generation and RhB degradation. This work offers a fresh insight in designing and synthesizing multi-structure heterojunction photocatalysts for extensive applications in the field of green and sustainable new energy.

## Conflicts of interest

There are no conflicts to declare.

## Acknowledgements

The authors acknowledge the National Natural Science Foundation of China (NSFC) (Grant No. 22175007, 52172080 and 21975007), National Natural Science Foundation for Outstanding Youth Foundation, the Fundamental Research Funds for the Central Universities, the National Program for Support of Top-notch Young Professionals, the 111 project (Grant No. B14009).

## Notes and references

- Q. Wang and Z. Yang, *Environ. Pollut.*, 2016, **218**, 358.
- X. Zhang, X. Chen and X. Zhang, *Proc. Natl. Acad. Sci. U. S. A.*, 2018, **115**, 9193.
- J. Chow, R. Kopp and P. Portney, *Science*, 2003, **302**, 1528.
- A. Ahmed, E. Abdalla and M. Shaban, *J. Phys. Chem. C*, 2020, **124**, 22347.
- Q. Wang, T. Hisatomi, Q. Jia, H. Tokudome, M. Zhong, C. Wang, Z. Pan, T. Takata, M. Nakabayashi, N. Shibata, Y. Li, I. Sharp, A. Kudo, T. Yamada and K. Domen, *Nat. Mater.*, 2016, **15**, 611.
- W. Li, X. Huang, T. Zeng, Y. Liu, W. Hu, H. Yang, Y. Zhang and K. Wen, *Angew. Chem., Int. Ed. Engl.*, 2021, **60**, 1869.
- J. Kosco, M. Bidwell, H. Cha, T. Martin, C. Howells, M. Sachs, D. Anjum, S. Lopez, L. Zou, A. Wadsworth, W. Zhang, L. Zhang, J. Tellam, R. Sougrat, F. Laquai, D. DeLongchamp, J. Durrant and I. McCulloch, *Nat. Mater.*, 2020, **19**, 559.
- Y. Wei, J. Wang, R. Yu, J. Wan and D. Wang, *Angew. Chem., Int. Ed. Engl.*, 2019, **58**, 1422.
- K. K. Khaing, D. Yin, S. Xiao, L. Deng, F. Zhao, B. Liu, T. Chen, L. Li, X. Guo, J. Liu and Y. Zhang, *J. Phys. Chem. C*, 2020, **124**, 11831.
- T. Senasu, S. Nijpanich, S. Juabrum, N. Chanlek and S. Nanan, *Appl. Surf. Sci.*, 2021, **567**, 150850.
- S.-G. Xia, Z. Zhang, J.-N. Wu, Y. Wang, M.-J. Sun, Y. Cui, C.-L. Zhao, J.-Y. Zhong, W. Cao, H. Wang, M. Zhang, Y.-C. Zheng and X.-B. Li, *Appl. Catal., B*, 2021, **284**, 119703.
- W. Tao, M. Wang, R. Ali, S. Nie, Q. Zeng, R. Yang, W.-M. Lau, L. He, H. Tang and X. Jian, *Appl. Surf. Sci.*, 2019, **495**, 143435.
- Z. Lin, B. Yu and J. Huang, *Langmuir*, 2020, **36**, 5967.
- Z. Niu, S. Yi, C. Li, Y. Liu, Q. Pang, Z. Liu and X. Yue, *Chem. Eng. J.*, 2020, **390**, 124602.





- 15 J. Liu, G. Liu, M. Li, W. Shen, Z. Liu, J. Wang, J. Zhao, L. Jiang and Y. Song, *Energy Environ. Sci.*, 2010, **3**, 1503.
- 16 Y. Liu, G. Xu and H. Lv, *J. Mater. Sci.: Mater. Electron.*, 2018, **29**, 10504.
- 17 S. Cho, C. Ahn, J. Park and S. Jeon, *Nanoscale*, 2018, **10**, 9747.
- 18 X. Wang, K. Maeda, A. Thomas, K. Takanabe, G. Xin, J. M. Carlsson, K. Domen and M. Antonietti, *Nat. Mater.*, 2009, **8**, 76.
- 19 X. W. Shi, M. Fujitsuka, Z. Z. Lou, P. Zhang and T. Majima, *J. Mater. Chem. A*, 2017, **5**, 9671–9681.
- 20 H. Wei, W. A. McMaster, J. Z. Y. Tan, D. H. Chen and R. A. Caruso, *J. Mater. Chem. A*, 2018, **6**, 7236–7245.
- 21 C. Marchal, T. Cottineau, M. G. Méndez-Medrano, C. Colbeau-Justin, V. Caps and V. Keller, *Adv. Energy Mater.*, 2018, **8**, 1702142.
- 22 X. Wang, F. Wang, B. Chen, K. Cheng, J. Wang, J. Zhang and H. Song, *Appl. Surf. Sci.*, 2018, **453**, 320.
- 23 X. Chen, J. Wei, R. Hou, Y. Liang, Z. Xie, Y. Zhu, X. Zhang and H. Wang, *Appl. Catal., B*, 2016, **188**, 342.
- 24 T. Zhao, Z. Liu, K. Nakata, S. Nishimoto, T. Murakami, Y. Zhao, L. Jiang and A. Fujishima, *J. Mater. Chem.*, 2010, **20**, 5095.
- 25 N. Wang, Y. Gao, Y. Wang, K. Liu, W. Lai, Y. Hu, Y. Zhao, S. Chou and L. Jiang, *Adv. Sci.*, 2016, **3**, 1600013.
- 26 G. Yue, S. Li, D. Li, J. Liu, Y. Wang, Y. Zhao, N. Wang, Z. Cui and Y. Zhao, *Langmuir*, 2019, **35**, 4843.
- 27 L. Lang, D. Wu and Z. Xu, *Chem.–Eur. J.*, 2012, **18**, 10661.
- 28 D. Li, F. Guo, Z. Cui, J. Zhou, Y. Zhai, Y. Du, J. Liu, N. Wang and Y. Zhao, *ACS Appl. Mater. Interfaces*, 2020, **12**, 53503.
- 29 D. Li, H. Li, S. Zheng, N. Gao, S. Li, J. Liu, L. Hou, J. Liu, B. Miao, J. Bai, Z. Cui, N. Wang, B. Wang and Y. Zhao, *J. Colloid Interface Sci.*, 2022, **607**, 655.
- 30 C. Han, Y. Wang, Y. Lei, B. Wang, N. Wu, Q. Shi and Q. Li, *Nano Res.*, 2015, **8**, 1199.
- 31 S. P. Adhikari, G. P. Awasthi, H. J. Kim, C. H. Park and C. S. Kim, *Langmuir*, 2016, **32**, 6163.
- 32 C. Wang, L. Hu, B. Chai, J. Yan and J. Li, *Appl. Surf. Sci.*, 2018, **430**, 243.
- 33 T. Wang, J. Xu, Z. Zhang, H. Bian, H. Xiao and T. Sun, *J. Mater. Sci.: Mater. Electron.*, 2020, **32**, 1178.
- 34 H. Wei, W. A. McMaster, J. Z. Y. Tan, L. Cao, D. H. Chen and R. A. Caruso, *J. Phys. Chem. C*, 2017, **121**, 22114.
- 35 H. L. Hou, L. Wang, F. M. Gao, X. F. Yang and W. Y. Yang, *J. Mater. Chem. C*, 2019, **7**, 7858.
- 36 C. B. Liu, L. L. Wang, Y. H. Tang, S. L. Luo, Y. T. Liu, S. Q. Zhang, Y. X. Zeng and Y. Z. Xu, *Appl. Catal., B*, 2015, **164**, 1.
- 37 J. Liu, D. Li, X. Liu, J. Zhou, H. Zhao, N. Wang, Z. Cui, J. Bai and Y. Zhao, *New J. Chem.*, 2021, **45**, 22123.
- 38 L. Lin, Z. Yu and X. Wang, *Angew. Chem., Int. Ed. Engl.*, 2019, **58**, 6164.
- 39 M. Rahman and C. Mullins, *Acc. Chem. Res.*, 2019, **52**, 248.
- 40 A. Khan and M. Tahir, *Appl. Catal., B*, 2021, **285**, 119777.
- 41 S. Kumar, A. Baruah, S. Tonda, B. Kumar, V. Shanker and B. Sreedhar, *Nanoscale*, 2014, **6**, 4830.
- 42 C. Hu, L. E, K. Hu, L. Lai, D. Zhao, W. Zhao and H. Rong, *J. Mater. Sci.*, 2019, **55**, 151.
- 43 Z. Huang, Q. Sun, K. Lv, Z. Zhang, M. Li and B. Li, *Appl. Catal., B*, 2015, **164**, 420.
- 44 J. Wang, G. Wang, X. Wang, Y. Wu, Y. Su and H. Tang, *Carbon*, 2019, **149**, 618.
- 45 W. Li, Q. Ma, X. Wang, X. Chu, F. Wang, X. Wang and C. Wang, *J. Mater. Chem. A*, 2020, **8**, 19533.
- 46 F. Li, X. Xiao, C. Zhao, J. Liu, Q. Li, C. Guo, C. Tian, L. Zhang, J. Hu and B. Jiang, *J. Colloid Interface Sci.*, 2020, **572**, 22.
- 47 L. Y. Lu, G. H. Wang, M. Zou, J. Wang and J. Li, *Appl. Surf. Sci.*, 2018, **441**, 1012.
- 48 H. Zhao, Y. Dong, P. Jiang, H. Miao, G. Wang and J. Zhang, *J. Mater. Chem. A*, 2015, **3**, 7375.
- 49 T. Wu, G. Liu and J. Zhao, *J. Phys. Chem. B*, 1998, **102**, 5845.
- 50 M. Rochkind, S. Pasternak and Y. Paz, *Molecules*, 2014, **20**, 88–110.
- 51 R. Hao, G. Wang, H. Tang, L. Sun, C. Xu and D. Han, *Appl. Catal., B*, 2016, **187**, 47.
- 52 L. Huang, H. Xu, Y. Li, H. Li, X. Cheng, J. Xia, Y. Xu and G. Cai, *Dalton Trans.*, 2013, **42**, 8606.
- 53 Z. Tong, D. Yang, T. Xiao, Y. Tian and Z. Jiang, *Chem. Eng. J.*, 2015, **260**, 117.
- 54 Y. Li, H. Zhang, P. Liu, D. Wang, Y. Li and H. Zhao, *Small*, 2013, **9**, 3336.
- 55 B. Chai, J. Yan, C. Wang, Z. Ren and Y. Zhu, *Appl. Surf. Sci.*, 2017, **391**, 376.
- 56 Y. Xu and M. A. A. Schoonen, *Am. Mineral.*, 2000, **85**, 543.

